# Two-dimensional distribution of As atoms doped in a Si crystal by atomic-resolution high-angle annular dark field STEM

T. Yamazaki
*Department of Physics, Science University of Tokyo, 1-3 Kagurazaka, Shinjuku-ku Tokyo 162-8601, Japan*

K. Watanabe
*Tokyo Metropolitan College of Technology, 1-10-40 Higashiohi, Shinagawa-ku, Tokyo 140-0011, Japan*

Y. Kikuchi
*Materials & Materials Engineering Laboratories, Fujitsu Laboratories Ltd., 10-1, Morinosato-Wakamiya, Atsugi, 243-0197, Japan*

M. Kawasaki
*Electron Optics Division, JEOL Ltd., 1-2 Musashino 3-chome, Akisima, Tokyo 196-8558, Japan*

I. Hashimoto
*Department of Physics, Science University of Tokyo, 1-3 Kagurazaka, Shinjuku-ku Tokyo 162-8601, Japan*

M. Shiojiri
*Department of Anatomy, Kanazawa Medical University, Ishikawa 920-0293, Japan*
*and Kyoto Institute of Technology, Kyoto 606-8585, Japan*
(Received 22 November 1999)

Observation of arsenic doped silicon has been made by using *Z*-contrast images of high-angle annular dark field scanning transmission electron microscopy with a tightly focused electron probe. The images show characteristic excess brightness depending on the number of arsenic atoms per atomic column. Through a simple analysis capable of identifying the number of arsenic atoms in an atomic column by using the above characteristic brightness, the quantitative two-dimensional distribution of arsenic atoms can be successfully obtained at atomic resolution, being consistent with the secondary ion mass spectroscopy and Rutherford backscattering spectroscopy measurements. This method is the only capable technique for detecting impurity atoms in every atomic column.

## I. INTRODUCTION

As well known, a transmission electron diffraction technique is the only capable method for studying local structure. Especially, high-resolution transmission electron microscopy (HRTEM) has been widely used to analyze many material structures such as defects and interfaces.[1–4] The technique depends on the coherent interference of scattered electrons, thus being difficult to directly interpret images due to effects of sample thickness and electron optical setting of a microscope.

Recently it has been possible, using a dedicated scanning transmission electron microscope (STEM),[5,6] to obtain incoherent images in resolution comparable to those of HRTEM. Crewe and Wall[7] and Issacson *et al.*[8] first measured a single atom and an atomic cluster on the amorphous layer with a STEM equipped with annular dark field (ADF) detector. An increase of inner detector angle progressively replaces coherent Bragg scattering with thermal diffuse scattering.[9] Loane, Kirkland, and Silcox[10] suggested the enhancement of contrast on an atomic column by channeling in a crystal, allowing the determination of impurity position with respect to the crystal lattice. The incoherent high-angle scattering is generated kinematically, even when a low-order diffraction is strongly dynamical, so that the images formed from this are almost independent of sample thickness and defocus. Combining the high-angle annular dark-field (HAADF) STEM with channeling of a wave packet in a low-order zone axis, Pennycook and Jesson[11] originated images of a perfect crystal atomic resolved, which can be intuitively interpreted without the need of simulations due to the absence of contrast reversal against defocus and sample thickness unlike the phase-contrast image of HRTEM. By improving the point-to-point resolution reaching 0.13 nm in addition to probe brightness, the method is now positively applied to many structures such as boundaries[12] and precipitates embedded in a matrix[13] as well as perfect structures. An additional advantage of the incoherent imaging method in STEM mode is that incoherent scattering is able to reveal a wealth of composition information, because the intensity is increased towards a $Z^2$ dependence of unscreening Rutherford scattering.[14,15] A detailed study of impurities inside a crystal, however, has not been performed positively although the demand for measuring impurity atom positions at nanometer area increases with a development of electronic devices.

It is the purpose of this paper to extend the capability of high-resolution *Z*-contrast images for identifying the number of impurity atoms in an atomic column by a simple analysis and to provide a two-dimensional distribution of impurity atoms at atomic resolution with a HAADF-STEM method. In Sec. II, experimental procedure is presented. The analysis is explained in Sec. III. Section IV is devoted to show the results and discussion. Finally the summary is given in Sec. V.

 

## II. EXPERIMENTAL PROCEDURE

Czochralski-grown [100]-oriented *p*-type silicon wafers with electrical resistivity of 10 Ω cm were used in the present experiment. The arsenic atom implantation was carried out at room temperature with 25 keV to a dose of $5\times10^{15}/\mathrm{cm}^2$. Rapid thermal annealing was performed at 1000 °C for 10 sec in dry $N_2$ atmosphere to avoid formation of residual defects. Samples were prepared by mechanical polishing and ion milling with 4-keV Ar ions. Since high-resolution images cannot be obtained with increasing amorphous and oxide surfaces, the ion milling was carefully done with angles as low as possible, and the final ion milling was done at 1.7 keV in order to remove the amorphous and oxide surfaces. Observations were carried out in the selected thin amorphous region. Hence, it is considered that the statistical error introduced by amorphous and oxide surfaces is not so essential for the determination of arsenic atom concentration from high-resolution images. HAADF-STEM observations were performed with a JEM-2010F-TEM/STEM, operated at 200 kV. High-resolution images were formed by scanning a probe across to the sample and by recording scattering electrons synchronously with an annular detector set from 50 to 110 mrad. The spherical aberration $C_s$ and the semiangle $\alpha$ of the probe were 1.02 mm and 6 mrad, respectively. The defocus value was selected to be −50 nm, corresponding to the Scherzer focus. Image processing was made by Fourier filtering, where the mask of 2-$\mathrm{nm}^{-1}$ diameter was used for each spot. The mask size, ranging from 2 to 3 $\mathrm{nm}^{-1}$, does not have much effect on the impurity determination. In order to confirm the ability of our method, a one-dimensional profile of arsenic atom concentration was measured with a Physical Electrics 6600 secondary-ion mass spectroscopy (SIMS). The concentration at 20 nm depth and the fraction of substitutional arsenic atoms were determined with a KOBELCO Mikro-*i* Rutherford backscattering spectroscopy (RBS).

## III. ANALYSIS

### A. Image calculation

In order to describe the thermal diffuse scattering of a wave packet for electron-beam channeling in a low-order zone axis, multiple scattering of electrons has to be taken into account. By using a high-angle annular detector, *Z*-contrast images are shown to be negligibly contributed from coherent scattering. Thus their intensity is proportional to integrated electron intensity at all atomic sites. For the calculation of the wave function, there are two main methods. One is the multislice method, in which a solution is given by the step-by-step integration based on optical physics,[16] being applied to various objects. It is, however, computationally inefficient since the multislice calculations in STEM mode[17,18] have been performed for each probe position to yield an integrated convergent-beam-diffraction intensity over an annular detector, while the $\beta$ approximation reduces computing time drastically.[19] An alternative method is called the Bethe eigenvalue method,[20,21] in which a wave function is written by three-dimensional Bloch waves. Its early approach was limited to a perfect crystal, but it is now expanded to multilayers and defects. Furthermore, it provides physical insight for understanding the image formation.[22,23] Pennycook and Jesson[11] clearly showed how incoherent images can be explained using the Bloch wave description of the coherent incident probe. Following in their description, the wave function $\Psi$ at an atomic site $(\mathbf{R}_i,z)$ due to a probe located at the surface $(\mathbf{R}_0,0)$ is given by

$$\Psi(\mathbf{R}_i-\mathbf{R}_0,z)=\sum_j A^j(\mathbf{R}_i-\mathbf{R}_0,z), \tag{1}$$

with

$$\begin{aligned}A^j(\mathbf{R}_i-\mathbf{R}_0,z)=&\int_{\text{probe}}\epsilon^j(\mathbf{K})\tau^j(\mathbf{R}_i,\mathbf{K})\exp\{i(k_z+\gamma^j)z\}\\&\times\exp(-\mu^j z)\exp\{i\mathbf{K}\cdot(\mathbf{R}_i-\mathbf{R}_0)\}\\&\times\exp\{iW(\mathbf{K})\}d\mathbf{K},\end{aligned} \tag{2}$$

where $A^j$ are amplitude contributions from each Bloch state $\tau^j$ integrated over all angles comprising the incident probe, $k_z+\gamma^j$ are transverse energies, $\epsilon^j$ are excitation amplitudes, and $\mu^j$ are absorption coefficients for each branch *j*. The lens aberration function $W(\mathbf{K})$ is given by

$$W(\mathbf{K})=\pi\lambda|\mathbf{K}|^2(\Delta f+\tfrac{1}{2}C_s\lambda^2|\mathbf{K}|^2), \tag{3}$$

where $\Delta f$ is the defocus and λ wavelength.[24]

If the $\delta$-function approximation is adopted, the intensity of images is represented by a simple sum over atomic sites,

$$I(\mathbf{R}_0,t)=\sum_i\int_0^t\sigma_i|\Psi(\mathbf{R}_i-\mathbf{R}_0,z)|^2dz, \tag{4}$$

where *t* is sample thickness and $\sigma_i$ are cross sections for high-angle thermal diffuse scattering calculated by the Einstein model. The deviation from the Einstein model is limited to within 20% for typical atomic spaces.[25] Scattering factors by Weickenmeir and Kohl[26] were used to calculate the real crystal potential and thermal diffuse scattering, because the Gaussian fit proposed by Doyle and Turner[27] is inaccurate for large scattering angles ($s>0.2\,\mathrm{nm}^{-1}$). Debye-Waller factors for silicon and arsenic are fixed to be 0.0045 and 0.0067 $\mathrm{nm}^2$.[28] Elastic scattering intensities and thermal diffuse scattering intensities for silicon and arsenic atoms are displayed in Fig. 1. Since the intensity of elastic scattering decreases with *s* due to the Debye-Waller factors, it is found that the main contribution in our annular range as shown by the two arrows in Fig. 1 is the thermal diffuse scattering for both materials. The cross section of arsenic atom is about 5.5 times larger than that of silicon. The relation between the cross sections for the detection range of 50–110 mrad and the atomic number squared $(Z_i)^2$ is displayed in Fig. 2. The cross section increases linearly with $(Z_i)^2$ in this angular condition. The *Z*-contrast intensity at each probe position is obtained to integrate the scattered electrons over the angular range.

### B. Estimation of impurity concentration

In order to identify the impurity atoms in the doped region by using characteristic brightness, intensity calculations were made by using two models. One model assumes that small impurity concentration does not affect greatly the Bloch wave field into the crystal and only changes the cross sec-

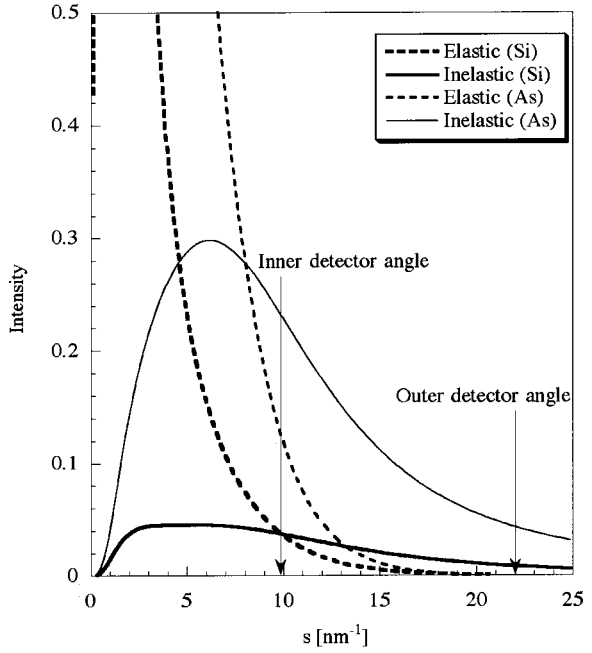


FIG. 1. Intensities of elastic and thermal diffuse scattering (TDS) from an isolated silicon atom and arsenic atoms. The two arrows show the position of the inner angle and outer angle for the detector.

tions of the thermal diffuse scattering. Thus the extra intensity due to an arsenic atom is determined by the cross section and the number of arsenic atoms. The intensity ratio on an atomic column is simply given by the ratio of the arsenic atom cross section to the silicon atom:

$$\frac{I_{\mathrm{Si(As)}}}{I_{\mathrm{Si}}}=\frac{\{N(1-x)\sigma_{\mathrm{Si}}+Nx\sigma_{\mathrm{As}}\}I}{N\sigma_{\mathrm{Si}}I}=(1-x)+x\frac{\sigma_{\mathrm{As}}}{\sigma_{\mathrm{Si}}}, \quad (5)$$

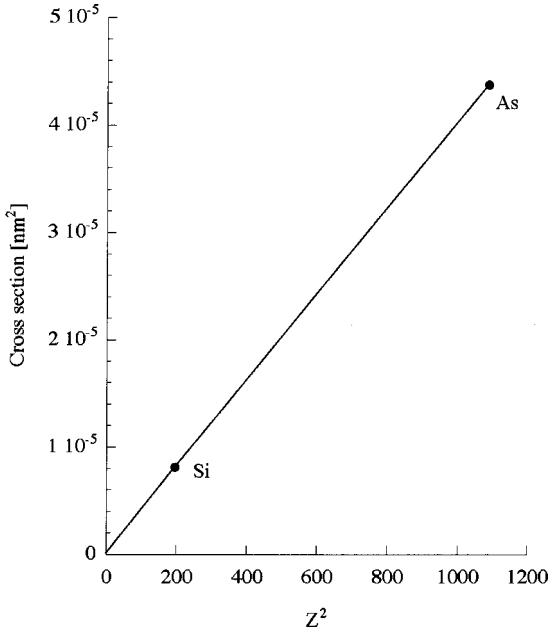


FIG. 2. The relation between the high-angle atomic cross section $\sigma_i$ of Si and As atoms and the atomic number square $Z_i^2$.

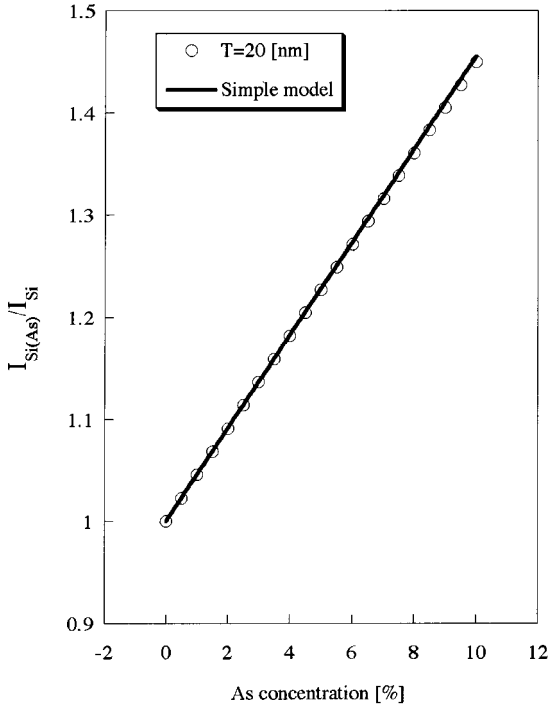


FIG. 3. The intensity on a column calculated by two models. The solid line shows the simulation using Eq. (6), and the open circles show the full dynamical simulation, respectively.

where $N$ is the number of silicon atoms on a column, $x$ is the concentration of arsenic atom, $\sigma_{\mathrm{Si}}$ and $\sigma_{\mathrm{As}}$ are cross sections of silicon and arsenic atoms, and $I$ is the averaged intensity of a propagating wave packet on an atomic column. Another model is based on the averaged potential, which is used to simulate disorder compounds.[29] Bloch waves are different from those in perfect silicon, so that simulations must be carried out with a supercell. But it is found that each atomic column contributes to the image independently of its neighbors until the main Bloch states overlap themselves,[30] and thereby the intensity on a participating column is calculated with a unit cell. The relation between extra brightness and arsenic atom concentration for two models are derived in Fig. 3. The intensities calculated by the two models agree well. In other words, the intensity change due to a few impurity atoms can be approximately calculated by the change of cross sections and the number of impurity atoms per column. By using the fact that the cross section is linearly proportional to $Z^2$, Eq. (5) is rewritten as

$$\frac{I_{\mathrm{Si(As)}}}{I_{\mathrm{Si}}}=(1-x)+x\frac{(Z_{\mathrm{As}})^2}{(Z_{\mathrm{Si}})^2}, \quad (6)$$

where $Z_{\mathrm{Si}}$ and $Z_{\mathrm{As}}$ are the atomic number of silicon and arsenic, respectively.

### C. Fitting procedure

Phenomenologically, a linear relationship between the number of electrons on the annular detector and the recorded intensities is assumed, so that the thickness-($t$) dependent intensity $I^{\mathrm{expt}}(t)$ is written by the theoretical values $I^{\mathrm{theor}}(t)$:

$$I^{\mathrm{expt}}(t)=AI^{\mathrm{theor}}(t)+B, \quad (7)$$

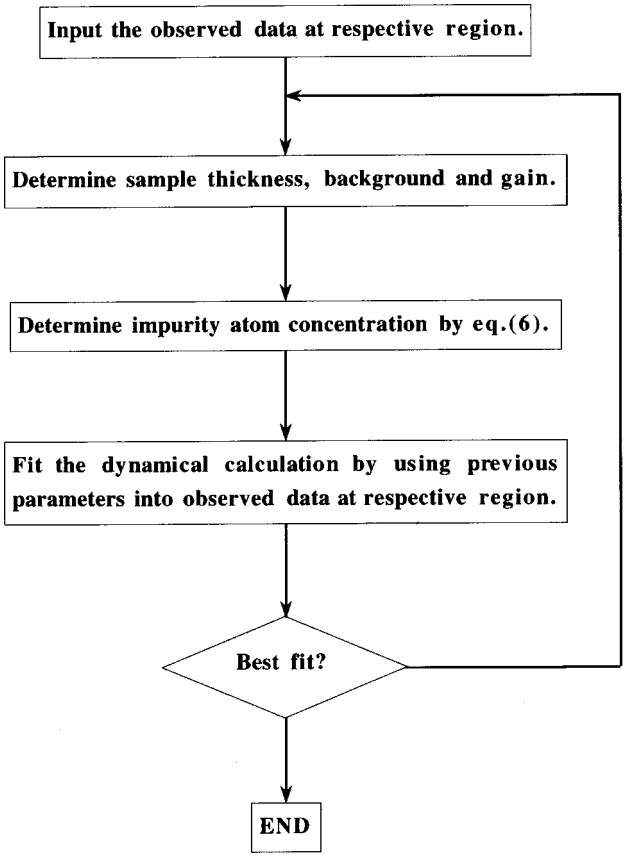


FIG. 4. Flow chart of a program for image and profile fitting.

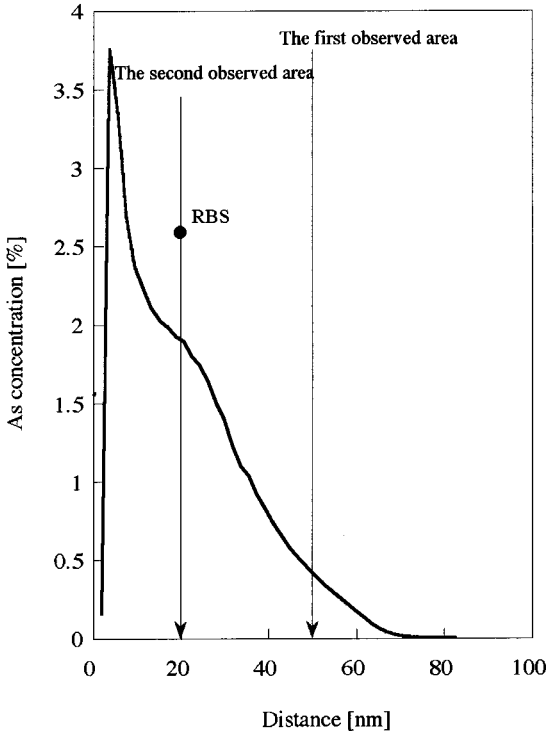


FIG. 5. One-dimensional profile of arsenic atoms measured with SIMS and the concentration measured with RBS. Measured positions indicated by arrows.

where $A$ is the gain and $B$ the background. For measurement, the area of uniform thickness was selected to confirm the same background and gain. Thus, at the first step, background, gain, and sample thickness are determined by fitting

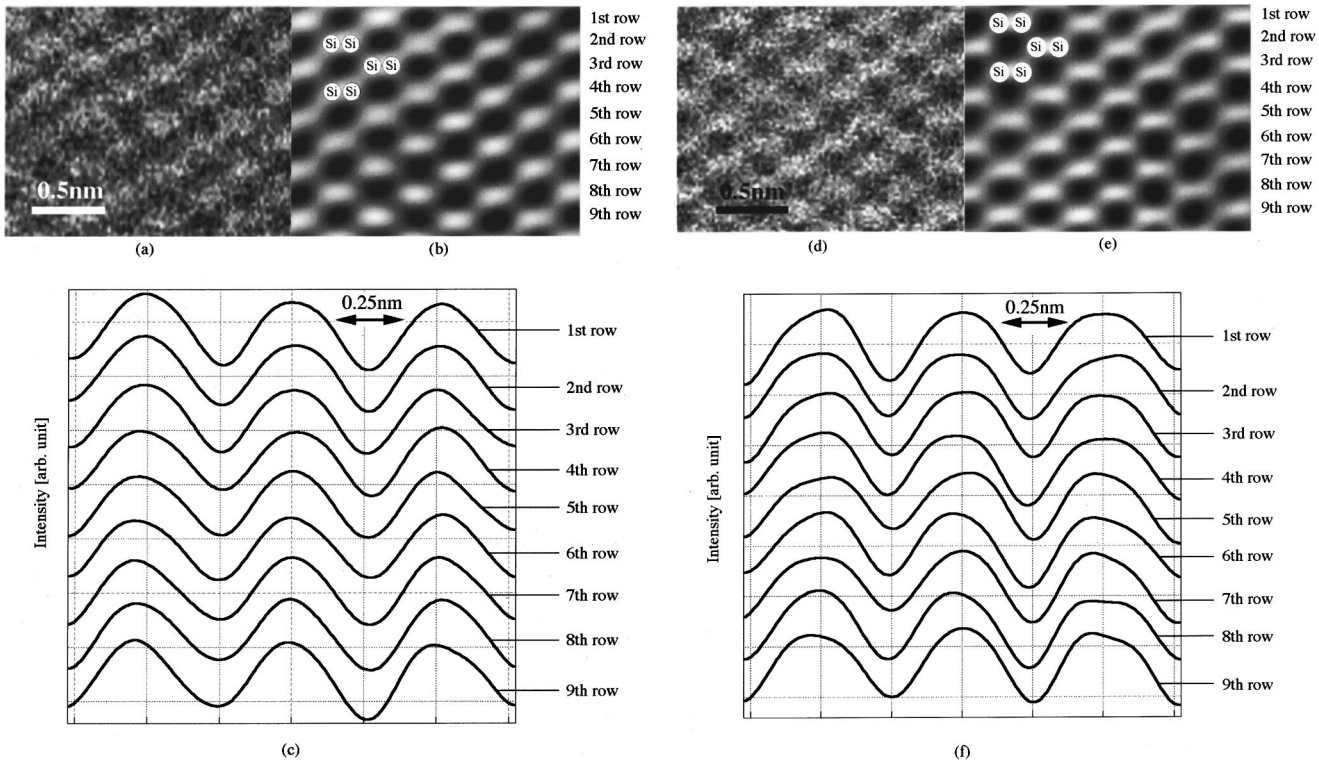


FIG. 6. (a) Observed *Z*-contrast image in the matrix, (b) its processed image, and (c) its line profiles along rows. (d) Observed *Z*-contrast image in the arsenic-doped region, (e) its processed image, and (f) its line profiles along rows.

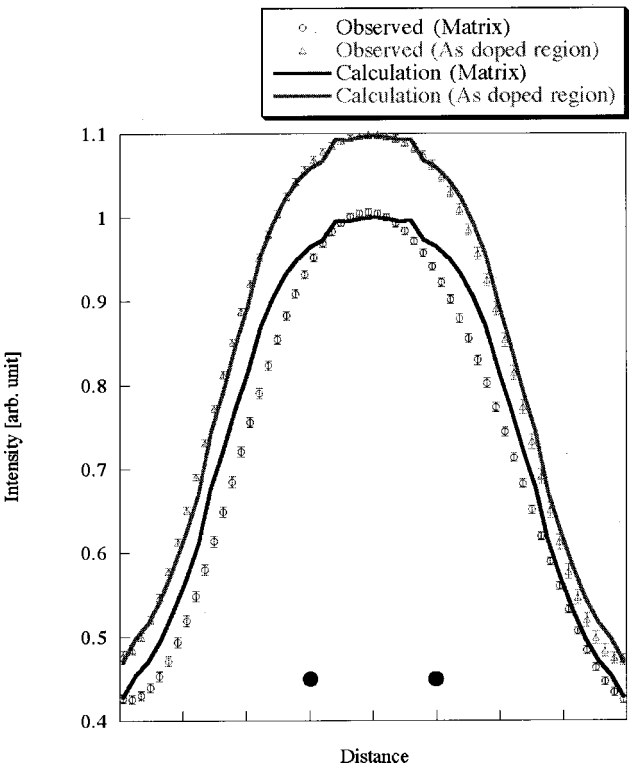


FIG. 7. Experimental intensity profiles that were deduced by averaging and processing 27 spots in the matrix and the arsenic-doped region and calculated intensity profiles. For the doped region, the averaged arsenic concentration is determined to be 2.1 at. %. The solid circles denote the positions of the atomic column.

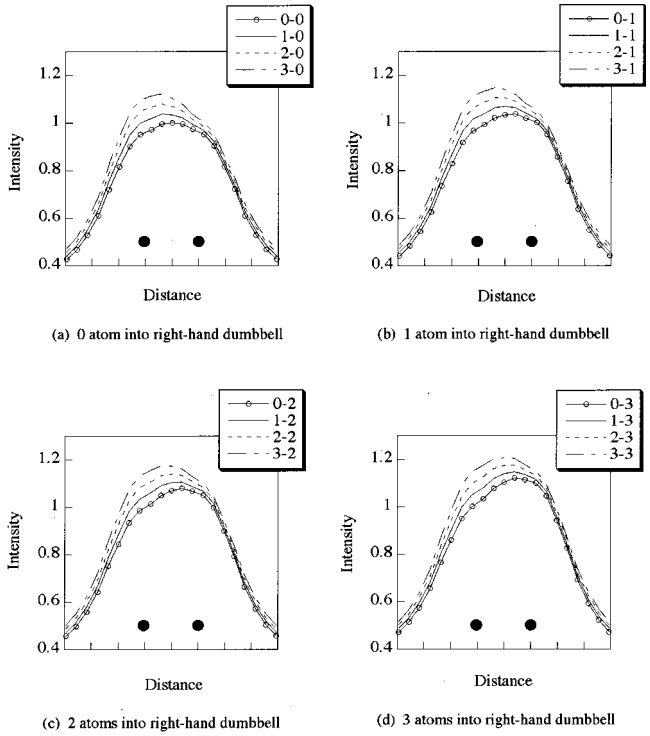


FIG. 8. The intensity of dumbbells, each of which is composed of two columns with various of arsenic atoms. The solid circles denote the positions of the atomic column.

dynamical simulations to averaged line profiles in a matrix. This step is indispensable for the measurement of simple substances that have no reference columns without impurity atoms. Next, the average arsenic atom concentration in a doped region is estimated from Eq. (6). At the third step, a dynamical fitting is made in the doped region on the basis of this concentration, leading to the final arsenic atom concentration. At the final step, the best fitting to line profiles is performed by using the intensity patterns on individual atomic columns depending on the arsenic atom number. Figure 4 shows the simplified flow chart in which only intensity profiles are measured in the matrix and the doped region. As for ordered compounds, impurity atom concentrations as well as background, gain, and thickness are simultaneously determined without references.

## IV. RESULTS AND DISCUSSION

Figure 5 shows one-dimensional profiles of arsenic atoms measured by SIMS and the concentration at 20 nm depth measured by the RBS technique together with the measured positions. The SIMS measurement indicates the concentration of arsenic atoms to be 0.5 and 1.9 at. % in the matrix and the doped regions, respectively. The RBS measurement gives 2.6 at. % for the arsenic atom concentration in addition to the fact that 78% of the arsenic atoms sit on the substitutional site. Like oxygen columns in $SrTiO_3$,[31] the excitation amplitudes of Bloch waves associated with interstitials in Eq. (2) are very small, so that the effect of interstitial atoms of 0.6 at. % concentration is neglected for the determination of substitutional arsenic atom concentration as the first approximation.[32]

The STEM images, processed images, and those line intensities in the matrix and the doped region are displayed in Fig. 6. This image processing gives rise to a valuable image by decreasing noise drastically and powerfully to draw detailed structure. In the matrix, symmetric bright spots on unresolved dumbbells are uniformly found. On the other hand, symmetric and asymmetric excess bright spots on unresolved dumbbells are seen in the doped region. Since the cross section of arsenic atoms is roughly 5.5 times larger than that of silicon atoms, the main contribution to characteristic excess brightness in the doped region is mainly not by surface roughness but by the number of arsenic atoms. In order to determine the background, gain, thickness, and concentration, 27 spots in Figs. 6(b) and 6(c) are averaged.

Figure 7 illustrates that the averaged profiles are in good agreement with simulated ones. The thickness is estimated to be 25 nm, which corresponds to 65 atoms per column. The thickness almost agrees with the value estimated by the zero-loss intensity of electron-energy-loss spectroscopy (EELS). The ratio of extra brightness in the doped region to that in the matrix is 1.09 on average. By using the fitting procedure method in Sec. III C, this extra value corresponds to arsenic atom concentration of 2.2 at. %. If positions of arsenic atoms in the column do not greatly influence the Bloch waves, the effect of impurity position on the concentration undergoes $\pm 0.5$ at. % change. The resultant concentration is roughly consistent with SIMS and RBS results, whether or not the position dependence is taken into account. In practice, the RBS measurement gives the substitutional arsenic atom concentrations of 2.0 at. %. This value agrees with our result well.

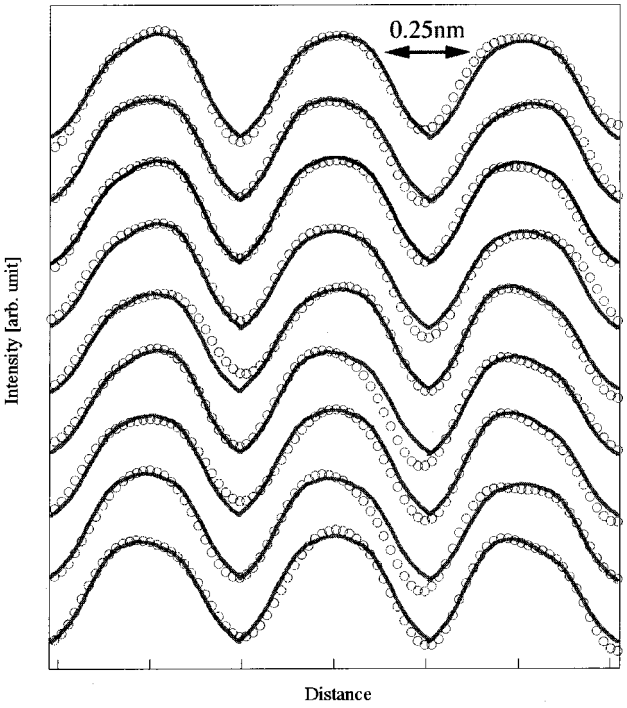


FIG. 9. Calculated (solid line) and experimental line profiles (circles) of processed images, corresponding to the profiles shown in Fig. 6(f).

The intensity patterns for dumbbells depending on the arsenic number in participating columns are shown in Fig. 8, where the number indicates arsenic atoms in an individual atomic column. By using these patterns, the result of best fitting to the experimental line profiles in the doped region in Fig. 6 are shown in Fig. 9. The nine simulated line profiles are approximately superimposed on experimental nine line profiles. From the results, two-dimensional distributions of arsenic atoms at atomic resolution are for the first time obtained as shown in Fig. 10. Since the matrix region at 50 nm depth still contains a few arsenic atoms as shown in Fig. 5, the arsenic atom concentration in the doped region becomes $2.2 \pm 1.0$ at. % by averaging over remaining matrix region.

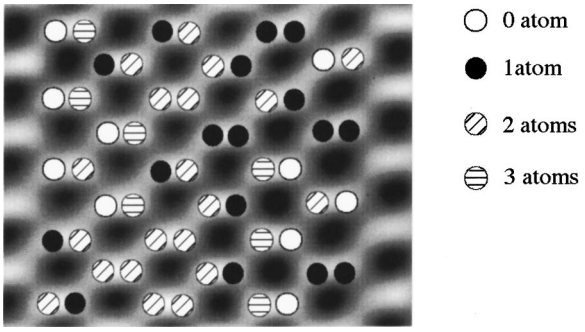


FIG. 10. Calculated two-dimensional distribution of arsenic atoms in the arsenic-doped region shown in Fig. 6(e).

## V. SUMMARY

Near-atomic column resolved *Z*-contrast images in the undoped and arsenic-doped silicon have been successfully presented with an tightly focused electron probe. The images show characteristic excess brightness depending on the number of arsenic atoms. Through the simple intensity analysis capable of identifying the number of arsenic atoms in an individual atomic columns with excess significant brightness, the two-dimensional distributions of arsenic atoms can be obtained at atomic resolution, being consistent with SIMS and RBS measurements. We believe that the method opens the way to measure two-dimensional distribution of impurity atoms at near atomic resolution. It is noteworthy to suggest that the ability to detect the arsenic atom concentration in the samples may be superior to that of either EELS or energy dispersive spectroscopy (EDS), although there is uncertainty of the position dependence of impurity atoms and the limit of the Einstein model.

[1] N. Uyeda, T. Kobayashi, E. Suito, Y. Harada, and M. Watanabe, J. Appl. Phys. **43**, 5181 (1972).
[2] S. Iijima, J. Appl. Phys. **42**, 5891 (1971).
[3] O. L. Krivanek, S. Isoda, and K. Kobayashi, Philos. Mag. **36**, 931 (1977).
[4] M. Shiojiri, C. Kaito, S. Sekimoto, and N. Nakamura, Philos. Mag. A **46**, 495 (1982).
[5] P. Xu, E. J. Kirkland, J. Silcox, and R. Keyse, Ultramicroscopy **32**, 93 (1990).
[6] H. S. von Harrach, Ultramicroscopy **58**, 1 (1995).
[7] A. V. Crewe and J. Wall, Science **168**, 1338 (1970).
[8] M. S. Issacson, J. P. Langmore, N. W. Parker, D. Kopf, and M. Utlaut, Ultramicroscopy **1**, 359 (1976).
[9] A. Howie, J. Microsc. **117**, 11 (1979).
[10] R. F. Loane, E. J. Kirkland, and J. Silcox, Acta Crystallogr., Sect. A: Found. Crystallogr. **44**, 912 (1988).
[11] S. J. Pennycook and D. E. Jesson, Phys. Rev. Lett. **64**, 938 (1990).
[12] M. F. Chisholm, A. Maiti, S. J. Pennycook, and S. T. Pantelides, Phys. Rev. Lett. **81**, 132 (1998).
[13] K. Mitsuishi, M. Kawasaki, M. Takeguchi, and K. Furuya, Phys. Rev. Lett. **82**, 3082 (1999).
[14] V. E. Cosslett, in *Possibilities and Limitations for the Differentiation of Elements in Electron Microscope, Quantum Electron Microscopy*, edited by G. F. Bahr and E. H. Zeitler (Williams and Wilkins, Baltimore, 1965), p. 271.
[15] C. J. Humphreys, R. Sandstrom, and J. P. Spencer, Scan Electron Microsc. Part II, 233 (1973).
[16] J. M. Cowley and A. F. Moodie, Acta Crystallogr. **10**, 609 (1957).
[17] E. J. Kirkland, R. F. Loane, and J. Silicox, Ultramicroscopy **23**, 77 (1987).
[18] K. Nakamura, H. Kuribayashi, K. Kanehiro, and N. Tanaka, J. Electron Microsc. **33**, 1 (1997).
[19] C. A. Anderson, C. R. Birkeland, C. R. Anstis, and D. J. H. Cockayne, Ultramicroscopy **69**, 83 (1997).
[20] H. A. Bethe, Ann. Phys. (Leipzig) **87**, 55 (1928).
[21] F. Fujimoto, J. Phys. Soc. Jpn. **14**, 1558 (1959).

[22] F. Fujimoto, Phys. Status Solidi A **45**, 99 (1978).
[23] K. Kambe, Ultramicroscopy **10**, 223 (1982).
[24] P. Hartel, H. Rose, and C. Dinges, Ultramicroscopy **63**, 93 (1996).
[25] D. E. Jesson and S. J. Pennycook, Proc. R. Soc. London, Ser. A **449**, 273 (1995).
[26] A. Weickenmeier and H. Kohl, Acta Crystallogr., Sect. A: Found. Crystallogr. **47**, 590 (1991).
[27] P. A. Doyle and P. S. Turner, Acta Crystallogr., Sect. A: Cryst. Phys., Diffr., Theor. Gen. Crystallogr. **24**, 390 (1968).
[28] N. Hashikawa, K. Watanabe, Y. Kikuchi, Y. Oshima, and I. Hashimoto, Phys. Status Solidi A **154**, 531 (1996).
[29] N. Tanaka and J. M. Cowley, Acta Crystallogr., Sect. A: Found. Crystallogr. **43**, 337 (1987).
[30] S. J. Pennycook and D. E. Jesson, Ultramicroscopy **37**, 14 (1991).
[31] M. M. McGibbon, N. D. Browning, M. F. Chisholm, A. J. McGibbon, S. J. Pennycook, V. Ravikumar, and V. P. Dravid, Science **266**, 102 (1994).
[32] P. D. Nellist and S. J. Pennycook, Ultramicroscopy **78**, 111 (1999).